

Nonlinear Self-Confined Plasmonic Beams:

Experimental Proof

Supporting Information

Tintu Kuriakose,[†] Gilles Renversez,^{*,‡,#} Virginie Nazabal,[¶] Mahmoud M. R.

Elsawy,[§] Nathalie Coulon,^{||} Petr Nĕmec,[⊥] and Mathieu Chauvet^{*,†,#}

[†]*FEMTO-ST Institute, CNRS, University of Bourgogne Franche-Comté, 15B avenue des Montboucons, 25030 Besançon, France*

[‡]*Aix-Marseille Univ, CNRS, Centrale Marseille, Institut Fresnel, 13013 Marseille, France*

[¶]*Univ Rennes, CNRS, ISCR (Institut des Sciences Chimiques de Rennes) – UMR 6226, 35000 Rennes, France*

[§]*Aix-Marseille Univ, CNRS, Centrale Marseille, Institut Fresnel, 13013 Marseille, France*

^{||}*Univ Rennes, CNRS, IETR (Institut d'Electronique et des Technologies du numérique) – UMR 6164, 35000 Rennes, France*

[⊥]*Department of Graphic Arts and Photophysics, Faculty of chemical Technology, University of Pardubice, Studentská 573, 53210 Pardubice, Czech Republic*

#corresponding author

E-mail: gilles.renversez@univ-amu.fr; mathieu.chauvet@univ-fcomte.fr

Contents

1	Structure fabrication	S3
2	Experimental characterizations	S3

3	Simulations: modal analysis with the finite element method	S4
4	Details of the nonlinear mode profiles	S5
4.1	Impact of the thickness d of the silica buffer on the nonlinear mode type . . .	S6
4.2	Impact of the total power on the nonlinear modes	S8
4.3	Evaluation of the opto-geometrical nonlinear factor η_x^{1D} and its ratio	S8
5	Impact of parameter variability for the nonlinear mode simulations of con- figuration I	S12
5.1	Influence of silica buffer layer thickness d	S12
5.2	Influence of n_2 and of the ratio $\eta_x^{1D}(\text{TM with PS})/\eta_x^{1D}(\text{TM without PS})$. . .	S12
6	Complementary simulation results for configuration II	S14
6.1	Propagation simulations for configuration II at low power	S14
6.2	Comparisons between experimental results and numerical simulations for con- figuration II as a function of the PS length	S15
7	Complementary results for configurations I, II, and III	S18
8	Discussion on the limitations of the SNLSE	S18
9	Numerical implementation of the nonlinear propagation equation	S21
10	Experimental results: TE polarization versus TM polarization without PSS	S21
11	Test of thermal effects	S23
12	Complementary discussion on the solitonic nature of the self-trapped waves	S25
13	Test of the spatial modulation instability as origin of the observed lateral peaks in the beam profiles	S27
	References	S29

1 Structure fabrication

The heterostructure fabrication was conducted in several steps. The chalcogenide glass target has been specially manufactured to accommodate RF sputtering magnetron deposition. First, a 3.6 μm thick $\text{Ge}_{28.1}\text{Sb}_{6.3}\text{Se}_{65.6}$ chalcogenide layer with a refractive index of 2.54 at 1.55 μm is deposited by RF magnetron sputtering method on an oxidized silicon wafer. The morphology and topography of the chalcogenide waveguides are characterized by SEM and AFM and showed no cracks with a RMS roughness of about 0.3 nm. The refractive index dispersion is determined by m-lines method and variable angle spectroscopic ellipsometry using Cody–Lorentz modeling. Then a 10 nm silica buffer layer is deposited, followed by a 32 nm gold evaporated layer which is patterned by photolithography. The deposition of the very thin SiO_2 layer is carried out by a sputtering deposition technique. Characterizations show that a good quality silica layer with the targeted thickness was obtained. A 32 nm gold nanolayer is chosen since it is thick enough to provide the plasmonic effect while it can be deposited to form a uniform good quality layer. The input and output faces of the samples are formed by cleaving the processed wafer according to the crystalline orientation of the silicon substrate. A previous study dealing with waveguides made from chalcogenide cores, fabricated with the same RF sputtering magnetron deposition method, on a silica layer deposited on a silicon substrate¹ has shown that, with this cleaving technique, the coupling losses mainly come from mode mismatch, Fresnel coefficient, surface roughness, and non-orthogonality of the facets with the waveguide propagation axis.

2 Experimental characterizations

Optical measurements are performed with a femtosecond optical parametric oscillator (Chameleon OPO from Coherent) set to 1550nm. The power is varied by the combination of a half wave plate and a polarizer. The latter component is also used to adjust the polarization state of the injected beam to either TM or TE. The laser beam is shaped into an elliptical spot

using a cylindrical lens and a x40 microscope objective to form 4 μm and 31 μm beam (FWHM) along X-axis and Y- axis, respectively. The beam profile at the output of the sample is imaged on a Vidicon camera with a x10 microscope objective. Input and output powers is monitored by power meters to deduce the coupling efficiency, the peak power and the waveguide transmission. Careful beam alignment is also performed to maximize the beam overlap with the fundamental mode of the planar waveguide and thus avoid excitation of higher-order modes. Observations at the output face of the structure confirms that the presence of higher order modes is negligible. The input spatial averaged incident intensity is determined by dividing the coupled light peak power by the elliptical section of the guided mode at the entrance face corresponding to waists of 1.21 μm along the X-axis and 30 μm along the Y-axis. In linear regime a $\sim 21\%$ waveguide transmission is measured for both TM and TE polarizations when light propagates away from the metallized area. This transmitted power is consistent with a coupling efficiency of 28% and propagation losses of about 0.19 cm^{-1} . To exclude the possible influence of thermally-induced self-focusing in nonlinear regime, experiments are repeated with a mechanical chopper after the light source to diminish the average power to 40% while keeping the same peak power. No measurable change is observed compared to the behaviour described in Figure 3 that excludes any significant role of the temperature (see Section 11 in this Supplement).

3 Simulations: modal analysis with the finite element method

FEM numerical simulations [32,33] are performed to compute the nonlinear fundamental modes in the structures with PS in order determine the optimum thicknesses for the investigated layered structure. For all modal calculations the investigated structure is assumed to be invariant along propagation. It reveals that the silica buffer thickness d is the most critical parameter for the design as expected from previous studies [19,20,34]. The pres-

ence of the metal marginally influences the mode distribution for thick silica layer (see Figure 2(a), for a silica buffer layer thickness $d = 30$ nm), as witnessed by the calculated profiles which are very similar to the one of the fundamental guided modes of a chalcogenide on silica slab waveguide. To the contrary, the TM mode profile is more and more affected by the metal as the silica buffer layer becomes thinner. For TM polarization, the studied metal/dielectric structure (Figure 1 (b)) supports a plasmon-soliton wave that extends into the nonlinear dielectric layer which is thus favorable to reveal the formation of a self-focused beam that takes advantage of the plasmon-enhanced Kerr effect. The propagation losses are weaker compared to the case of the extremely confined plasmonic waves present at a basic metal-dielectric interface. The FEM simulations provide an optimal thickness, in terms of nonlinearity enhancement and propagation losses, of 10 nm for the silica buffer layer. For this designed multilayer structure the plasmon-soliton propagation length approaches 350 μm when computed from the measured losses in the PS.

It is worth mentioning that since the x and y field profiles of the 2D plasmon-soliton nonlinear wave are coupled, the observed localization along the X-axis (Figure 2(b), TM polarization) is associated with an enhanced localization along the Y-axis (See Section 4 of this Supplement).

4 Details of the nonlinear mode profiles

We can compute the nonlinear vector modes that propagate in a waveguide or photonic structure with a Kerr nonlinearity region as a function of the mode power using the model we have already developed using the finite element method (FEM) and the fixed power algorithm² (see previous section) based on Maxwell's equations. In this section we focus on two issues: the impact of the thickness d of the silica buffer layer between the gold layer and the chalcogenide nonlinear layer on the type of modes, and the impact of the power carried by the nonlinear solution on the modes distribution.

4.1 Impact of the thickness d of the silica buffer on the nonlinear mode type

As already stated (see main article and quoted references), the thickness d of the silica buffer plays a key role in the mode type independently of the considered linear or nonlinear regimes. In Figure 2 of the main article, only profiles of the modulus squared of the electric field (intensity) along the X-axis for $y = 0$ are provided for the main TE and TM modes for two silica buffer thicknesses d . In Figure S1, a 3D view of the intensity profiles of the nonlinear modes with the same carried total power for $d = 10$ nm and $d = 30$ nm is given.

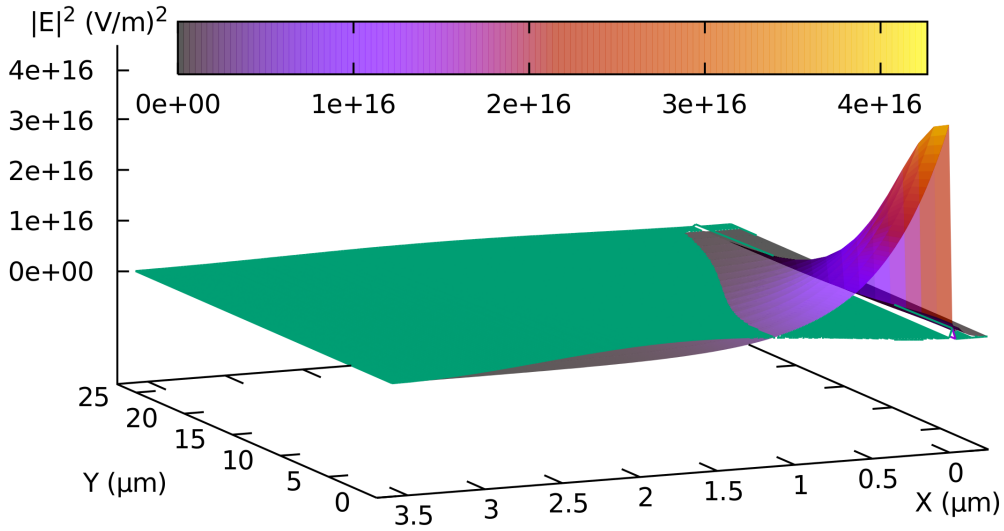


Figure S1: Intensity distribution of the nonlinear TM modes (only one half shown thanks to the symmetry axis along $y = 0$) for $d = 10$ nm (with color scale) and for $d = 30$ nm (green) with the same total power $P_{tot} = 513$ W. The vertical scale is identical for the two modes. Note that for $d=10$ nm, the distribution in the silica buffer layer is not shown due to its large value as shown in the profile provided in Figure 2 of the main article. See Figure S2 for the view of the distribution in the full structure.

First, Figure S1 shows the 2D localization of the investigated modes induced by the nonlinearity especially along the Y axis despite the absence of any permittivity contrast in

this direction in the initial structure. Second, this figure also clearly illustrates the stronger localization of the electric field of the TM mode for a PS with a silica buffer layer of $d = 10$ nm thickness (see Figure S2 for a full view of this TM mode) compare to a PS with $d = 30$ nm. It is this stronger spatial localization for both along the X-axis and the Y-axis that makes the improvement of the effective nonlinearity for the TM mode in presence of the PS compare to the ones of the three other cases studied experimentally in the main article: TM mode without PS, TE mode with and without PS.

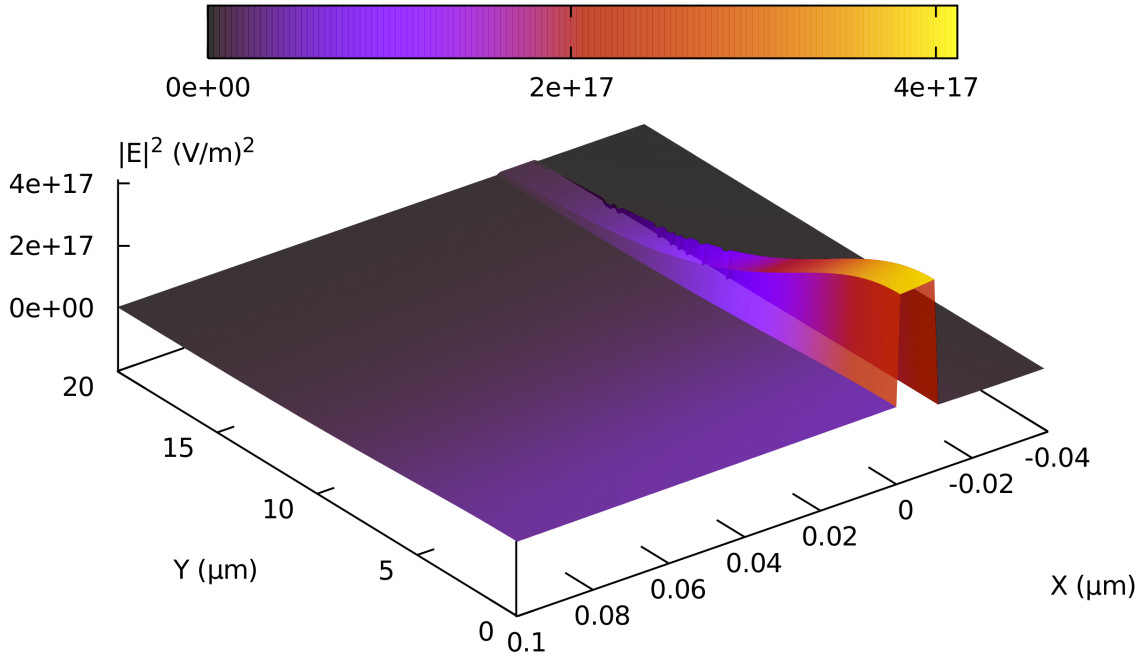


Figure S2: Intensity distribution of the nonlinear TM modes propagating inside the full PS for $d=10$ nm with a total power $P_{tot} = 513$ W (only one half shown thanks to the symmetry axis along $y = 0$). Note that due to the large values of the intensity in the silica buffer layer, the intensity in the other regions are not well resolved (see Figure S1 for details of these regions.)

For completeness, in Figure S3, we provide a full 3D view of the intensity profiles of the TM and TE nonlinear modes for the same total power of $P_{tot} = 513$ W for $d = 30$ nm. One can see that both polarizations have similar features in term of localization as stated in the main article.

4.2 Impact of the total power on the nonlinear modes

In nonlinear regime (at high intensity), the shape of the mode field profiles depends on the carried power. Two normalized intensity profiles of the nonlinear TM modes computed for $P_{tot} = 513$ W and $P_{tot} = 1108$ W are shown in Figure S4.

Along the X-axis, the mode width dependence on power is weak since it is mainly dictated by the layers layout (see Table 1 in the next section for a quantitative impact of this power dependence). The impact of power on the Y-axis FWHM is stronger but there is no need to insert this width in the propagation equation (3) since this equation describes by itself the focusing effect along the Y-axis due to the nonlinearity. Note that these FEM results cannot be compared directly with the experimental ones. Indeed, experimentally the propagation also includes the progressive beam reshaping toward a soliton profile since the input beam is fairly focused on the input facet of the structure and does not correspond to the self-coherent solution corresponding to the computed nonlinear modes.

4.3 Evaluation of the opto-geometrical nonlinear factor η_x^{1D} and its ratio

In table 1, the opto-geometrical nonlinear factor η_x^{1D} is provided as a function of the polarization case (TE or TM) and of the total power for the configuration corresponding to the experiment (silica buffer layer thickness $h = 10$ nm and gold thickness of 32 nm, see the Design and fabrication of the structures Section for the other parameters). The computed plasmonic enhancement of the nonlinearity, as measured by the ratio $\eta_x^{1D}(\text{TM with PS}) / \eta_x^{1D}(\text{without PS})$, is slightly above 3 and increases slowly with the power.

Table 1: Opto-geometrical nonlinear factor η_x^{1D} and their ratio, for the main TE and TM modes with and without the PS for several values of the mode total power and a silica buffer layer thickness $h = 10$ nm.

P_{tot} (W)	513	1108	2216
η_x^{1D} TM with PS	1.23	1.26	1.37
η_x^{1D} TE with PS	0.40	0.40	
η_x^{1D} TM without PS	0.39	0.39	0.39
η_x^{1D} TE without PS	0.40	0.40	
ratio η_x^{1D} TM with PS/ η_x^{1D} TM without PS	3.15	3.23	3.51

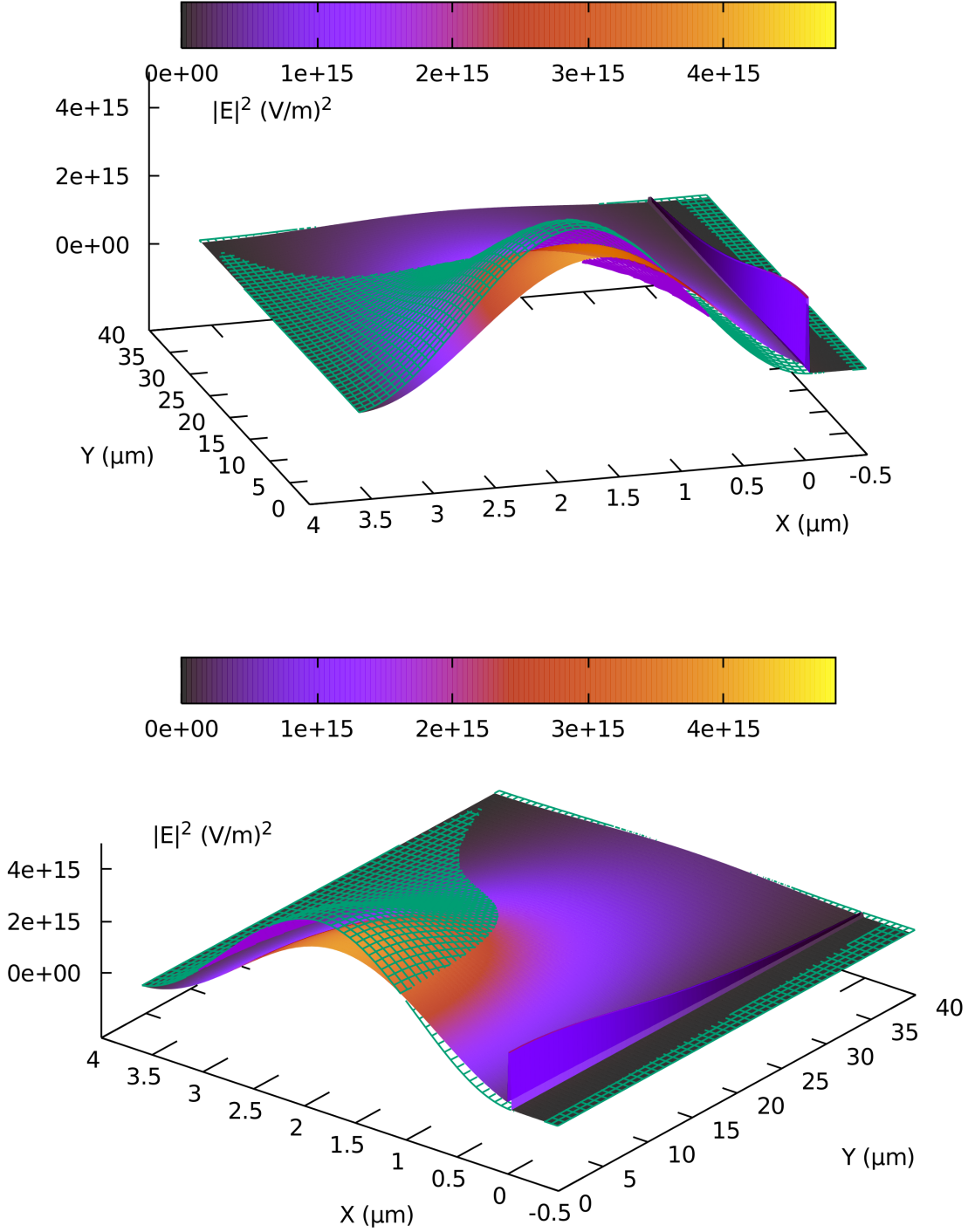


Figure S3: Intensity profiles of the nonlinear TM and TE modes for $d = 30$ nm and a power $P_{tot} = 513$ W seen from two view-points. The TM mode is shown with the color scale while the TE mode is shown using the green mesh. The vertical scale is the same for the two modes.(only one half shown thanks to the symmetry axis along $y = 0$)

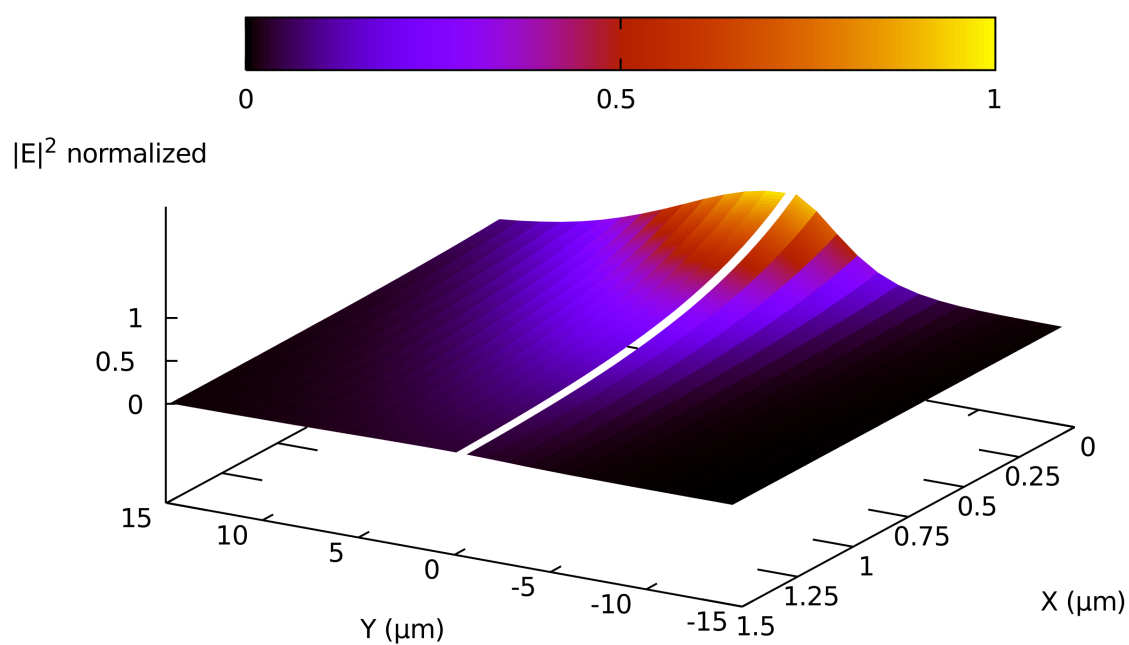


Figure S4: Normalized intensity distribution of the nonlinear TM modes for two different powers P_{tot} for $d = 10$ nm: $P = 513$ W on the left part (positive Y), $P = 1026$ W on the right (negative Y). (only one half shown thanks to the symmetry axis along $y = 0$)

5 Impact of parameter variability for the nonlinear mode simulations of configuration I

In this section, we describe the impact of parameters values on the simulations results describing configuration I.

5.1 Influence of silica buffer layer thickness d

We describe the influence of the silica buffer thickness when it is below the critical size ensuring a plasmonic behaviour for the TM mode with the PS. The targeted thickness d of 10 nm was obtained in the fabricated sample (see Figure 1(c) in the main article). Nevertheless, it is possible that this thickness d is not constant along the fabricated PS. For instance, if $d = 8$ nm instead of 10 nm, the corresponding mode for $P=513$ W changes compared to the one computed for $d = 10$ nm: the η_x^{1D} is now equal to 1.56 instead of 1.23. This implies that the ratio $\eta_x^{1D}(\text{TM with PS})/\eta_x^{1D}(\text{TM without PS})$ increases from 3.2 to 4. Consequently, the effective nonlinearity is increased when d decreases from 10 nm to 8 nm nevertheless it must be kept in mind that in the same time the propagation losses increase by 34 %.

5.2 Influence of n_2 and of the ratio $\eta_x^{1D}(\text{TM with PS})/\eta_x^{1D}(\text{TM without PS})$

In Figure S5, the FWHM is computed from nonlinear propagation simulations for configuration I as a function of the input beam intensity for several sets of n_2 and ratio $\eta_x^{1D}(\text{TM with PS})/\eta_x^{1D}(\text{TM without PS})$ values including the one given in Figure 6(b) of the article (purple curves shown in Figure S5). As explained in the Section 'Simulations: nonlinear propagation' of the article, the ratio $\eta_x^{1D}(\text{TM with PS})/\eta_x^{1D}(\text{TM without PS})$ controls the effective nonlinearity in the PS segment of the full structure. As stated in Ref. [22], for a GeSbSe chalcogenide glass of similar composition and for an identical laser source as in the

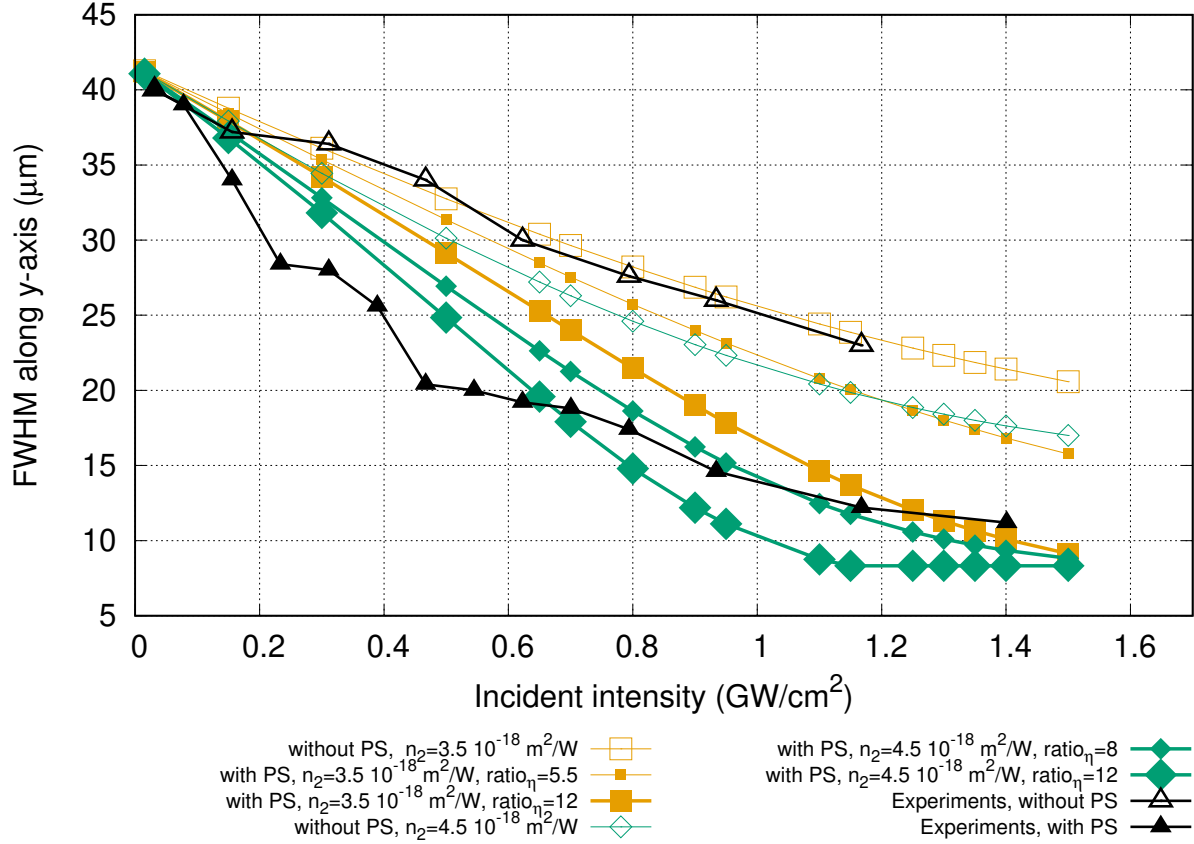


Figure S5: Comparison of the computed FWHM for configuration I as a function of the input beam intensity for several sets of n_2 and $\eta_x^{1D}(\text{TM with PS})/\eta_x^{1D}(\text{TM without PS})$ ratio values, the experimental results are also shown in black for the TM case with (filled triangles) and without PS (empty triangles).

present study, the estimated uncertainty on n_2 is 28.5%. This statement induces that the n_2 value is typically in the interval $[4 - 7] 10^{-18} \text{ m}^2/\text{W}$.

One can see that the simulation results differ only quantitatively and that the FWHM variations stay in the correct range. To simplify the discussion in the article, we use the n_2 value provided by the corrected results from Ref. [22] *i.e.* $5.5 10^{-18} \text{ m}^2/\text{W}$ but one can see that if we choose $4.5 10^{-18} \text{ m}^2/\text{W}$, we obtain simulation results (green curves in Figure S5) nearest to the experimental results (black curves in Figure S5).

6 Complementary simulation results for configuration II

6.1 Propagation simulations for configuration II at low power

In Figure 5, we provide a color map of the beam intensity evolution along the Y-axis versus propagation distance inside the full structure for the TM polarization for configuration II with $h=500 \mu\text{m}$ for an input average intensity of $1.25 \text{ GW}/\text{cm}^2$.

In order to complete these results and to validate the effect of the input intensity an additional color map is given in Figure S6 for the same parameters except an input incident average intensity of $15 \text{ MW}/\text{cm}^2$.

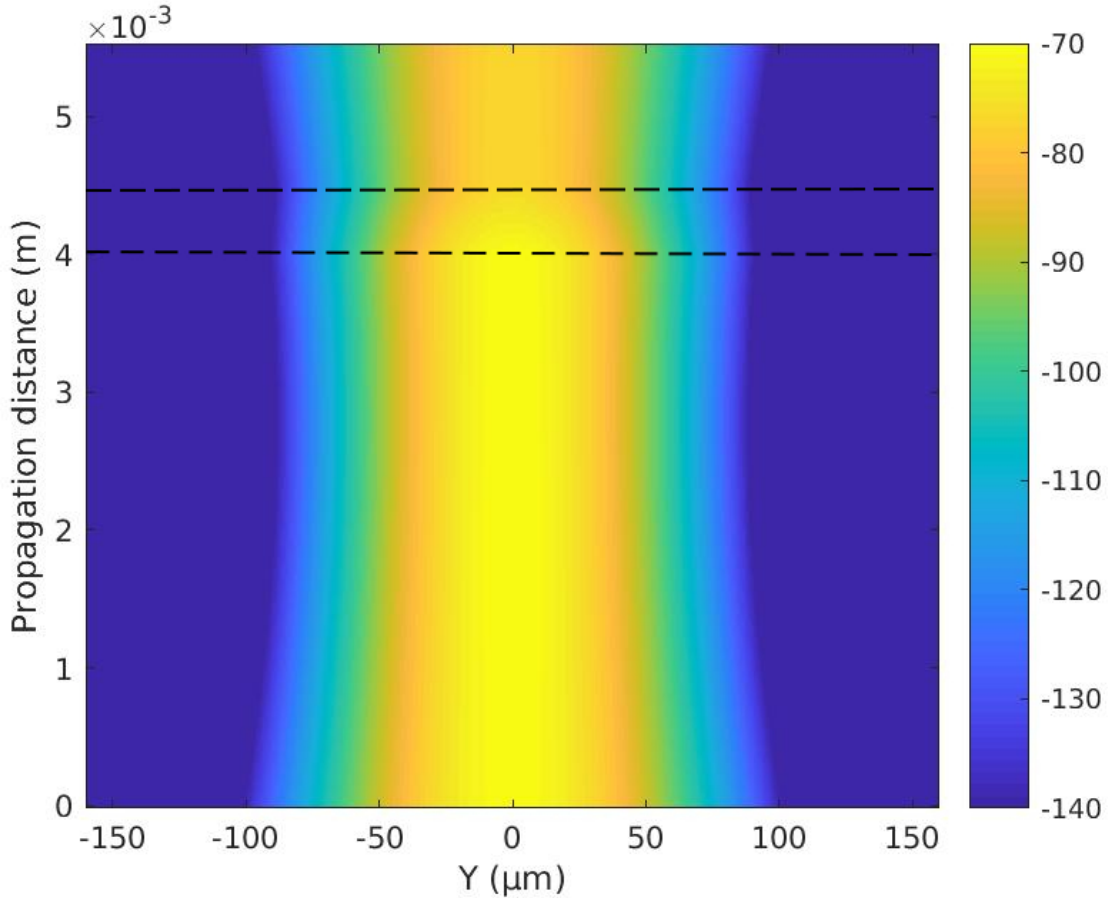


Figure S6: Color map in log scale of the beam intensity profile along the Y-axis versus propagation coordinate inside the full structure for a TM polarization for configuration II with $h=500 \mu\text{m}$. Input intensity of $15 \text{ MW}/\text{cm}^2$. The dashed line represents the limits of the PS.

In this figure, one can first see the focusing of the input beam on the initial section of the full structure (before the PS). This weak focusing is mainly due to the phase profile of the input beam³ since we imposed a spatial chirp to take into account the beam focusing induced by the microscope objective used to couple light in the structure. The same spatial chirp is used for all the propagation simulations of this study.

Second, a focusing effect is visible under the PS structure region attributed to the enhanced nonlinearity. Note that such a self-focusing takes place even for such a low intensity. Third, as the beam exits from the PS, a defocusing occurs due to the combination of the power loss induced by the higher propagation losses in the PS region and of the enhancement-free nonlinearity present away from the PS.

6.2 Comparisons between experimental results and numerical simulations for configuration II as a function of the PS length

In Figure S7, we compare the experimental results and numerical simulations for configuration II as a function of the length h of the PS. The FWHM of the output intensity profile in the Y-direction is depicted as a function of the incident average intensity for three different lengths h of the PS (see Figure 1(a)-(b) in the main article).

One can see that, for the largest h equal to $500\text{ }\mu\text{m}$, the computed Y-axis FWHM of the beam at the output facet of the full structure are in fair agreement with the experimental results. Nevertheless, it must be pointed out that the profiles along Y-axis are no longer simple Gaussian or hyperbolic secant at high intensities. In the high power regime, the profiles have multiple symmetric peaks as observed experimentally (Figure 5 in the main article) and numerically (Figure 6 in the main article). Consequently the FWHM is neither sufficient nor fully adequate to describe the features of the beam profile along the Y axis. The reported defocusing of the output beam observed experimentally for the highest intensities is also linked to the generation of these lateral peaks. This is seen above $1\text{ GW}/\text{cm}^2$ for configuration II for $h = 500\text{ }\mu\text{m}$ both in the experiments and in the simulations. Note that this defocusing

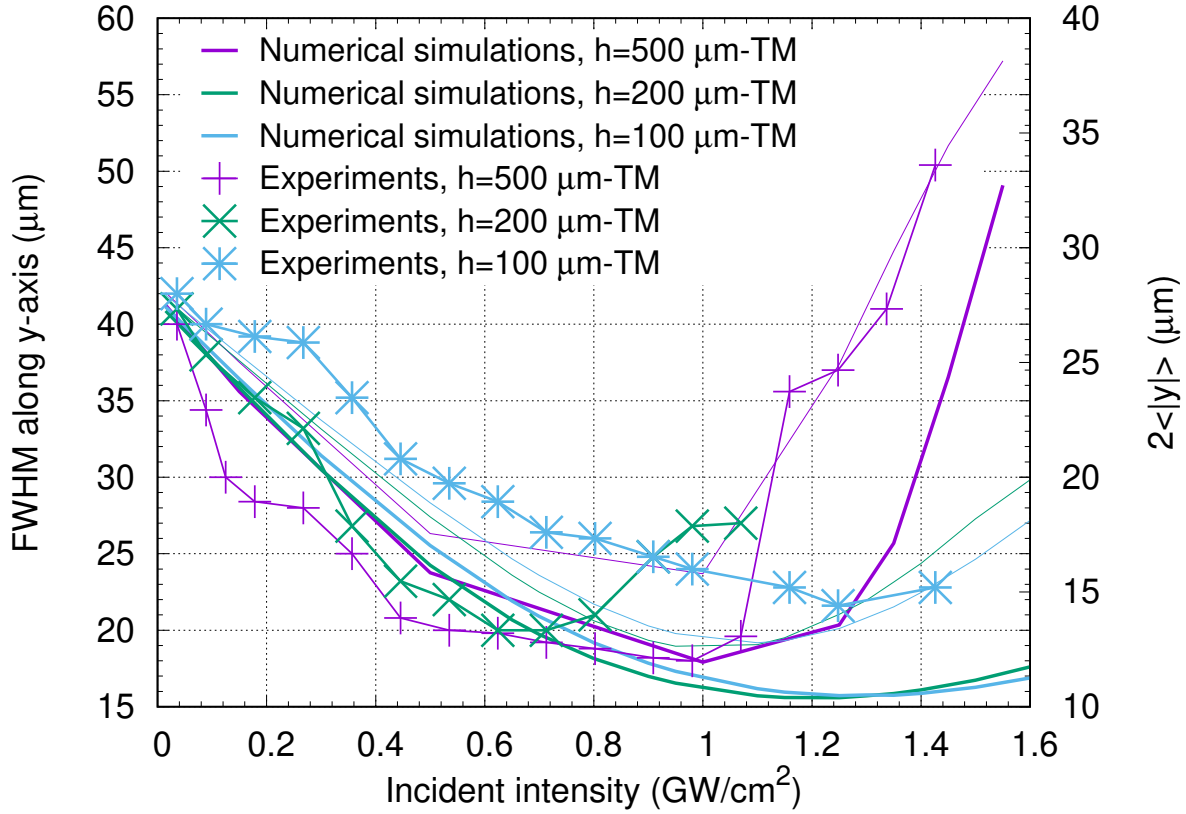


Figure S7: Computed and measured output beams FWHM along Y-axis for configuration II as a function of the input intensity for three different length h of the PS. On the right vertical scale, the corresponding computed mean full width $2\langle|y|\rangle$ of the output beam along the Y-axis are given (see the text for its definition) using thin curves.

effect was not seen in the FWHM experimental results in configuration I. The main reason is that the PS is located at the imaged output face of the full structure and consequently no diffraction can occur contrary to configuration II where the beam propagates some distance in the dielectric structure before its analysis. Nevertheless, when we increase the power of the input beam in the numerical simulations above $2 \text{ GW}/\text{cm}^2$ in configuration I for $h = 660 \mu\text{m}$, the generation of small lateral peaks are observed similarly as for configuration II. We infer that in the experiments for configuration I, the intensity reaching the PS structure is too low to induce the lateral peaks, and consequently the broadening regime of the beam is not yet reached.

For $h = 200 \mu\text{m}$, one can see that the measured and simulated results are also in good

agreement up to 0.8 GW/cm². Above this intensity, the simulations cannot reproduce the increase of the FWHM followed by a short plateau (only two experimental points for this plateau). For $h = 100 \mu\text{m}$, the experimental curve exhibits a gradual decrease followed by a final stabilization of the measured FWHM of the output beam. As already mentioned at the beginning of section 6.2 and as illustrated in Figure 5 of the article, the beam profiles contain multiple lateral peaks when the incident intensity becomes large. When this regime starts, on one hand the numerical FWHM values do not reflect the beam spreading since the smaller lateral peaks do not modify the FWHM values, on the otherhand the FWHM values of the experimental beams with their more irregular shapes take into account the beam spreading more rapidly. Consequently, the discrepancies between the experimental results and the numerical simulations increase with the incident intensity, up to the intensity requested to generate sufficiently high lateral peaks that modify the numerical FWHM values.

To allow our simplified model to take into account at least qualitatively the impact of the multiple lateral peaks on the spatial spreading of the output beam widths along the Y -axis we compute the quantity $2 \langle |y| \rangle$ defined by:

$$2 \langle |y| \rangle \equiv 2 \int_{Y\text{-section}} |y| |E|^2(y, z_{out}) dy / \int_{Y\text{-section}} |E|^2(y, z_{out}) dy$$

where z_{out} is the z -coordinate of the output face of the full structure. This quantity $2 \langle |y| \rangle$ corresponds to the mean full width along the Y -axis of the symmetric profiles under investigation, it can capture the influence of the multiple lateral peaks even if their maximum values do not reach the half maximum of the central peak. The corresponding curves for the three structures we studied in configuration II ($h = 500, 200, 100 \mu\text{m}$) are the thin ones in Figure S7 linked to the right vertical scale. As it can be seen, the results are in better agreement qualitatively with the experimental data than the direct output of the simulated FWHM. They show that the increase of the width of the output beam appears for smaller values of the incident intensities compared to the results given by the simulations of the

FWHM, even if quantitatively the increase observed for $h=200\text{ }\mu\text{m}$ as a function of the incident intensity is not obtained from $0.7\text{ GW}/\text{cm}^2$ but from $1.1\text{ GW}/\text{cm}^2$.

7 Complementary results for configurations I, II, and III

In Figure S8, we provide the comparisons of the computed and measured Y-axis FWHM output beams for the three configurations I, II, III for the largest h value of each configuration as a function of the input beam intensity. As it can be seen, the computed FWHM curves follow partially the ones of the experimental data except for configuration III where the incident intensity of the PS segment is larger due to the shorter distance (1 mm) between the input facet of the structure and the PS compared to configuration II (4 mm) and configuration III (4.5 mm). For configuration III, the numerical results don't show any increase for the FWHM. Nevertheless, if we look at the results provided by mean full width $2 < |y| >$ of the output beam, we see that we obtain a better qualitative agreement for the comparisons, for configurations I and II the simulation results stay globally correct while, for configuration III, we get the expected increase of the output beam width even if it appears for larger incident intensities compared to the experimental data.

8 Discussion on the limitations of the SNLSE

In this section, we extend the discussion summarized in the main article. It must be pointed out that the validity of our model does not extend to very high intensities and does not take into account the 200 fs time duration of the experimental light pulses. A spatio-temporal modeling of the nonlinear propagation would represent a valuable improvement of the current model. Comparisons between experiments realized with different pulse durations would also help to improve our understanding of the interplay between the different physical mechanisms controlling light propagation in these nonlinear structures. Indeed, in addition to the influence of higher order nonlinearities, the uncertainties on the considered nonlinear

parameters (n_2 , α_2) may have a larger impact as one moves away from the linear regime. Furthermore, the hypothesis on the propagation model themselves are also becoming less and less valid as the incident intensity increases. A full treatment of the Kerr nonlinearity considering the Maxwell's equations a⁴⁻⁶ is more adequate than the Schrödinger equation. We must also remind that in the present form the solved SNLSE includes only one mode in the description of the nonlinear wave propagation as it is the case in the simple NLSE where the waveguide is usually assumed to be single-mode⁷. At high intensities this description may be no longer valid.

The limitations of the SNLSE can also be at the origin of the observed discrepancies between the simulations results and the experimental ones. As an example, for configuration

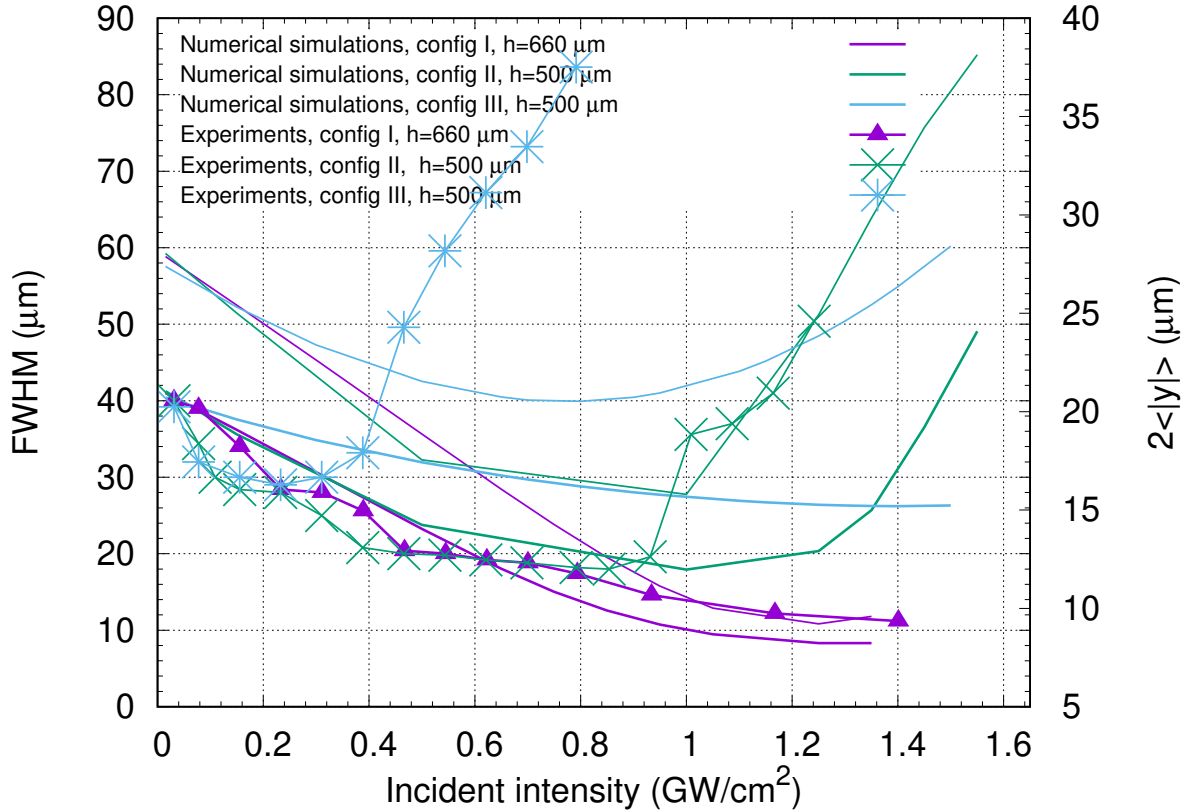


Figure S8: Computed and measured Y-axis FWHM output beams for the three configurations I, II, III as a function of the input beam intensity. On the right vertical scale, the corresponding computed mean full width $2 \langle |y| \rangle$ of the output beam along the Y-axis are given (see the text for its definition) using thin curves.

I and II, even if the numerical spatial profiles for the fields contain symmetric multipicks like the recorded ones and have quite similar FWHM, they differ quantitatively: their lateral peak positions being more distant to the beam center than the experimental ones for the same incident intensity. This phenomenon is similar to the predictions of 2D FDTD simulations of homogeneous Kerr media in which above some intensities the incident beam does not form a unique spatial soliton but a central peak with several lateral beams (see appendix C in⁸). Nevertheless, it is well known the SNLSE do not properly describe propagation with wavevectors that are not paraxial and that the validity worsens as the amplitude of the considered transverse wavevector³ is getting larger. The configurations considered in Figure 4(b) for $h=500$ nm and 4(c) for the three TM cases, and in Figures S7 and S8 for configurations II et III involve such large transverse wavevector components after the PS explaining why our model can only catch the quantitative behaviour of the measured output FWHM in these cases. Nonlinear FDTD simulations, eventually 3D ones, are needed to investigate more precisely these differences. Ultimately, the full numerical study of the self-trapped waves should be realized within a nonlinear 3D approach. A supplementary reason not mentioned above comes from the layered geometry of the investigated structure. In our 2D SNLSE model the impact of the layered structure (along the X axis) is only taken into account through the opto-geometrical nonlinear factor η_x^{1D} , the weak variation of the propagation constants and the losses. The computational resources to realize such 3D FDTD simulations is huge due to the large sizes of the studied structures. For a homogeneous cartesian grid of $\lambda/10$ sampling at $\lambda = 1.55 \mu m$ and considering only half of the structure thanks to the symmetry properties, the order of magnitude of cells is $5 \cdot 10^6$. This estimation is done without taken into account the grid size to correctly describe the nanoscale silica buffer and gold layers (10 grid cells to described the silica layer thickness means a 1 nm grid size, to be compared to the $0.155 \mu m$ of the coarser grid). Consequently, such simulations cannot be realized efficiently realized without a non-uniform grid nonlinear 3D FDTD software. Furthermore, the above estimations do not consider the supplementary computational cost generated by

the treatment of the nonlinearity in the FDTD code as it is explained in reference⁹.

9 Numerical implementation of the nonlinear propagation equation

We solve Eq. (3) using the Runge Kutta method of order 4 with the Interaction Picture (RK4IP) method, initially designed to solve the NLSE in the temporal domain, but adapted in the present case to the spatial domain since the RK4IP method has been proven to be more accurate and more efficient than the split-step Fourier method¹⁰. This task is relatively straightforward since there is no spatial dispersion to take into account due to the fact that we investigate only the beam propagation at a single wavelength ($1.55 \mu\text{m}$) while to solve the time equation one must take into account the frequency dependency of material properties to get accurate results. In addition to improve the efficiency of our numerical implementation, we have used the local error adaptative step size method that allows to adapt continuously the spatial step size in the propagation direction but keeping the local error below a fixed threshold¹¹. We have already used it successfully to study supercontinuum generation in highly nonlinear chalcogenide microstructured optical fibers¹².

10 Experimental results: TE polarization versus TM polarization without PS

Preliminary experiments have been performed to study the self-focusing behavior in the sample in the absence of metallic layer (without PS). The sample thus forms a slab waveguide with a guiding layer constituted of the chalcogenide glass. Beam self-trapping experiments have been realized for both TM and TE polarizations. The results presented in Figure S9 confirm that the self-focusing behavior is not dependent on the light polarization. This expected behavior contrasts with the situation of a sample with a metallic layer (with PS structure)

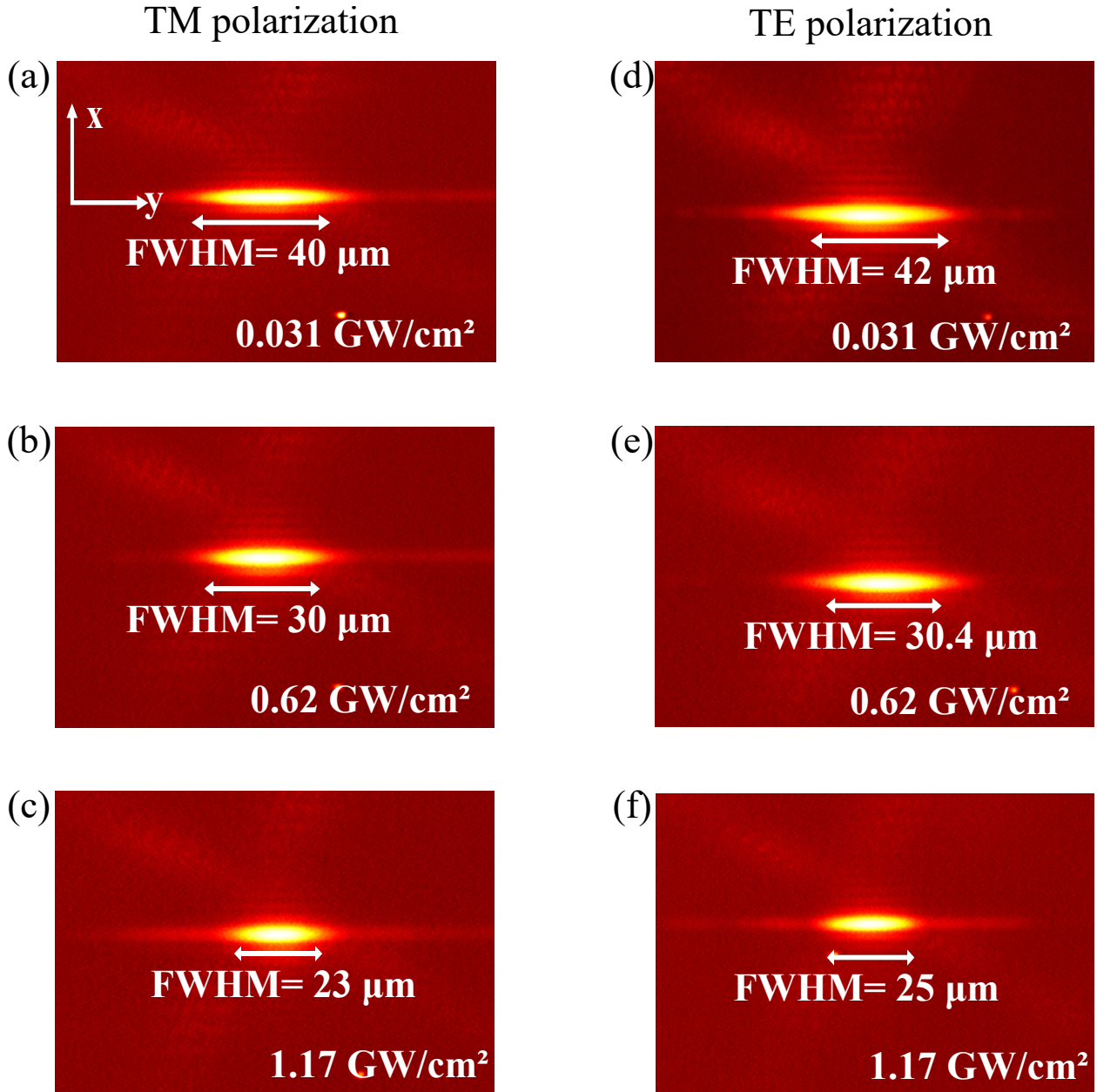


Figure S9: Experimental output images showing soliton formation and self-focusing behaviour without PS in a 5.1 mm long sample for TM and TE polarizations.

described in the article. We can unambiguously conclude that the strong dependence on polarization is due to the presence of the plasmonic structure.

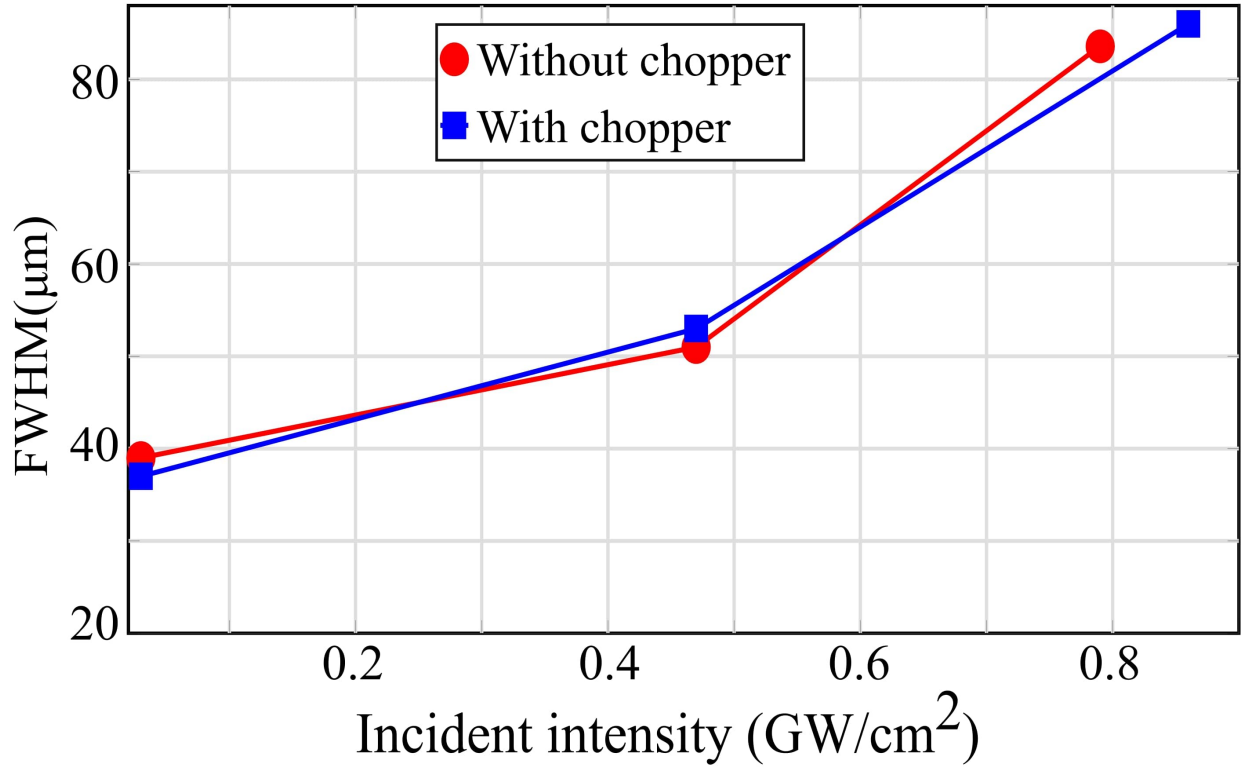


Figure S10: Evolution of the output beam FWHM as a function of incident intensity for configuration III with and without optical chopper.

11 Test of thermal effects

The influence of artefacts such as acoustic or thermal effect when using pulsed laser for z-scan experiments have been studied in Refs.^{13–15}. These works closely related to our experiment show that acoustic effect is negligible when pulse duration is shorter than acoustic transit time $t_a = \frac{w}{v_s}$. For beam size $w = 20 \mu\text{m}$ and sound velocity close to 2500 m/s in chalcogenide¹⁶, t_a is evaluated to 10 ns. In femtosecond regime, acoustic effect is thus not expected to play a role. Concerning the thermal diffusion, the characteristic time constant is given by $t_c = \frac{w^2}{4D}$. The diffusion constant D of GeSbSe was recently evaluated¹⁷ to $0.1 \text{ mm}^2/\text{s}$ which leads to $t_c = 1 \text{ ms}$. Since t_c is much longer than the spacing between pulses (12.5 ns) thermo-optical effect due to cumulative heating could be present. The development of a model taking into account the contribution of the photo-thermal effect in our complex configuration is out of the scope of this work but several experimental facts corroborate a negligible thermal

impact. First, nonlinear effect of bulk chalcogenide GeSbSe samples were characterized in Ref.¹⁸ both with the z-scan technique in single pulse ps regime at $1.06\ \mu\text{m}$ and with the self-trapping method at $1.55\ \mu\text{m}$ with the same femtosecond source as in the present study. Despite the high repetition rate used in this second method, it gave nonlinear coefficients (n_2 and two photon absorption coefficient) consistent with the first method, without the need for thermal correction. In a second step, the self-trapping technique with the femtosecond source was also developed to characterize the nonlinearities in GeSbSe films¹⁹. To check the influence of thermal effect in this slab configuration, the self-focusing response with and without a mechanical chopper was studied. While this optical modulation at 1 kHz with a duty cycle of 28% (0.28 ms long pulses train) does not change the pulse peak power, it should strongly reduce the thermal effect¹⁵ since it divides the average power by a factor larger than 3 and it also limits the cumulative heating since the modulation period is similar than t_c . However, no measurable difference of the focusing strength was noticed under the presence of modulated which led us to the conclusion that the Kerr effect is the dominant focusing effect. At last, for the present experiment, a thermal contribution could be expected due to the larger losses induced by the plasmonic effect. Beam modulation with a mechanical chopper has thus been reiterated. The results obtained in configuration III with a $500\ \mu\text{m}$ long PS (Figure S10) clearly show that, within the experimental errors, the strong light-induced diffraction observed in this particularly sensitive configuration is not modified in the presence of the modulated light at 1 kHz with a 40% duty cycle (0.4 ms pulses train followed by 0.6 ms without light). It is then fair to conclude that the Kerr self-focusing overcomes any photo-thermal effect.

12 Complementary discussion on the solitonic nature of the self-trapped waves

As already stated in the introduction, the terminology plasmon-soliton has been coined in Ref.²⁰ and has subsequently been used to name self-trapped nonlinear plasmonic waves in the numerous following articles dealing with these waves (Ref. [17-24] of the main article). In their simplest version, such a nonlinear wave couples together a plasmonic part in a linear medium and a solitonic part in a nonlinear medium both sharing the same propagation constant. When theoretical models are considered two main cases can be distinguished: the first one corresponds to lossless configurations ensuring stable propagation at least for some parameter sets, the second one corresponds to configurations where the loss (imaginary part of the metal permittivity) is taken into account (Ref. [20-22] main article). For this latter case, the stability property is not fulfilled mathematically inducing the loss of the solitonic nature of the wave. The plasmon-soliton can however form and maintain a nearly constant profile over a distance dictated by propagation losses. Such considerations about the stable nature of the generated nonlinear waves is not new, it has already been discussed many times such as in the book by Dauxois and Peyrard²¹ including in their conclusion entitled “Physical solitons, do they exist?”. Plasmon-solitons perfectly fit with their remarks since they lose the mathematical stability characteristic as soon as metal loss, inherently present, are taken into account in the nonlinear wave propagation. Nevertheless, our simulations show that the self-trapped characteristics are maintained over few hundred of micrometers when linear (mostly generated by the metal) and nonlinear loss parameters (two-photon absorption) are considered. This characteristic length scale must be compared with centimeter long dielectric waveguides used in typical Kerr spatial soliton experiments²². The difference comes from the high loss value above 120 dB/cm in the former case due to the plasmonic effect while it is approximately 1 dB/cm in the latter.

Another feature of the studied configurations is the inhomogeneity of the structures

along which the nonlinear wave propagates. In configuration I, there is a single straight interface that separates the fully dielectric nonlinear structure to the one with the PS where the effective nonlinearity is reinforced, the output face of this structure being in air. In configurations II and III, there are two interfaces: the second one separates the enhanced nonlinearity region to the normal nonlinearity one. In all the realized propagation simulations related to the experiments, the first secondary peaks emerge symmetrically around the central peak near the second interface or just after it.

To illustrate this discussion with a result directly related to our experiment we provide in Figure S11 a zoom of the nonlinear propagation of a beam with an input intensity of 1.1 GW/cm^2 in the PS for configuration I (PS at the end of the structure). As it can be seen, just after the beginning of the PS, the nonlinear wave starts to focus due to the enhanced effective nonlinearity then after approximately $370 \text{ }\mu\text{m}$ it starts to stabilize. The profile of the propagating nonlinear wave, not far from a plasmon-soliton, is then nearly conserved but as already stated due to the high losses induced for TM waves by the metal layer of the PS, this profile cannot maintain over long distance.

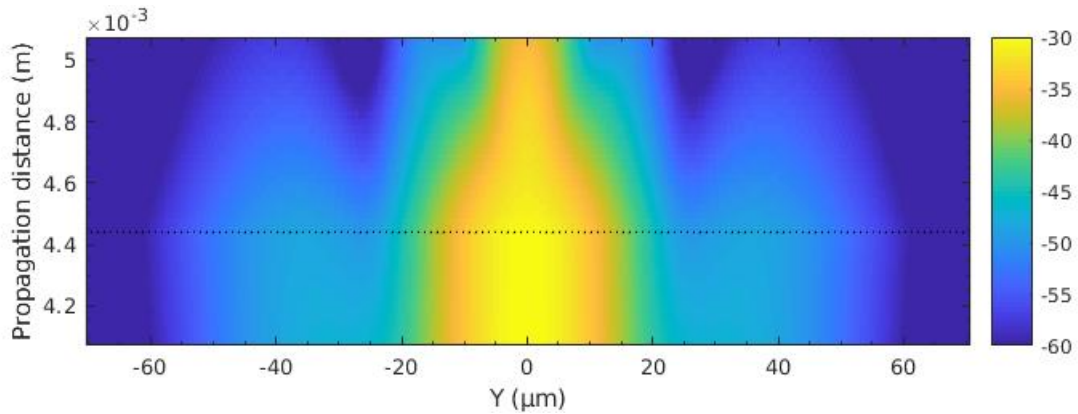


Figure S11: Color map in log scale of the beam intensity evolution along the Y-axis versus propagation at the end of the full structure for TM polarization for configuration I with PS length $h = 660 \text{ }\mu\text{m}$ in nonlinear regime (input intensity of 1.1 GW/cm^2). The dotted lines represent the limits of the PS.

To complete this discussion, we can evaluate the different characteristic physical lengths of our experiment: the diffraction length $L_D = 2\beta\sigma^2$ where β is the propagation constant

and σ is the beam width at $1/e$, the nonlinear length $L_{NL} = k_0 n_2 I$ where $k_0 = 2\pi/\lambda$, and the loss length $L_\alpha = 1/\alpha$ where α is the linear loss coefficient. For a gaussian beam we have $\sigma = FWHM/(2\log(1 + \sqrt{2}))$, for a typical example we choose $FWHM = 20 \mu\text{m}$ (*i.e.* between the $30 \mu\text{m}$ of the spatial soliton regime in the studied structure without PS and the $12 \mu\text{m}$ of the smallest observed beam in the structure with PS), and taking $\beta \simeq n_0 = 2.54$, we obtain $L_D = 1325 \mu\text{m}$. For an intensity of $1 \text{ GW}/\text{cm}^2$, and $n_2 = 5.5 \cdot 10^{-18} \text{ m}^2/\text{W}$ at $\lambda = 1.55 \mu\text{m}$, we obtain $L_{NL} = 4485 \mu\text{m}$. But if we consider the enhanced nonlinearity we increase n_2 by a factor 8 and if we choose an intensity of $1.5 \text{ GW}/\text{cm}^2$, we have $L_{NL} = 373 \mu\text{m}$. For the loss length, if we consider the structure without PS the measured linear loss coefficient is 0.19 cm^{-1} we get $L_\alpha = 52 \text{ mm}$ for, and if we consider the structure with PS: the measured linear loss coefficient is 28 cm^{-1} , we have $L_\alpha = 360 \mu\text{m}$. These results explain quantitatively why it is not possible to get stable plasmon-soliton in our experiment since within the structure with PS $L_\alpha \sim L_{NL} \ll L_D$ nevertheless the plasmon-soliton concept is fully useful to understand some of the observed phenomena and to build an approximated model. It is worth noting that this brief analysis does not describe all the phenomena since it does not take into account the discontinuities of the investigated structures (the interfaces between regions with or without PS) where important phenomena occur.

13 Test of the spatial modulation instability as origin of the observed lateral peaks in the beam profiles

In this section, we investigate if the observed symmetric multiple secondary peaks in the beam spatial profiles from the study of configuration II (see Figure 5 in the article) can be generated by the spatial modulation instability phenomenon. We used the results from Ref.²³ that gives explicit formula for the modulation instability gain and spatial frequency. In the framework of the SNLSE (see Section 8 for its limitations), the spatial frequency Λ_{max} associated to the maximum gain of the modulation instability is given by the following

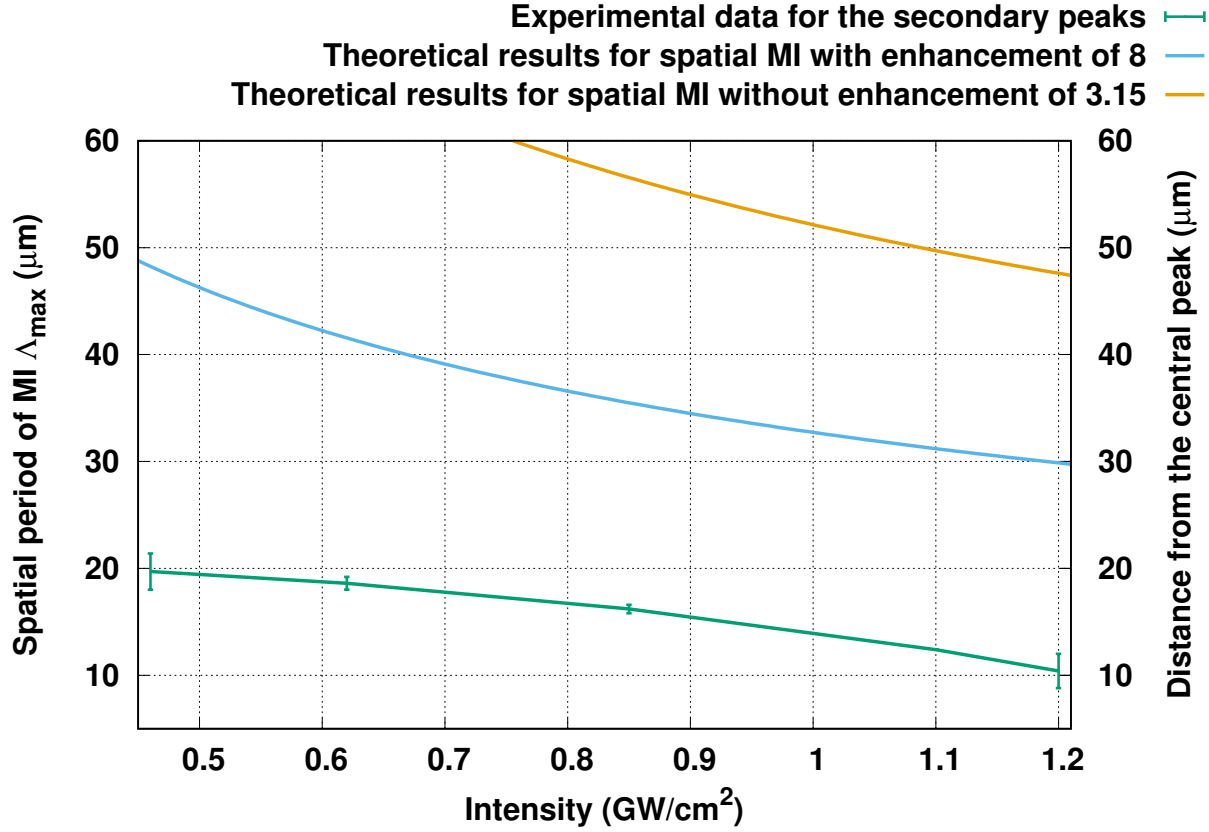


Figure S12: Experimental distance measured between the lateral secondary peak and the central peak (green) for the configuration II and theoretical spatial period Λ_{max} calculated from modulation instability for effective nonlinear coefficients enhancement of 8 (blue curve) and 3.15 (orange) versus input intensity. The error bars for the experimental data (green) are obtained from the left and right lateral peak distances relative to the central peak.

relations:

$$\Lambda_{max} = \frac{2\pi}{K_{max}} \text{ where } K_{max} = (2k_0\beta n_{2,eff}I)^{1/2} \quad (1)$$

where $k_0 = 2\pi/\lambda$, β is the propagation constant, I is the beam intensity, and $n_{2,eff}$ is the effective Kerr nonlinear coefficient. In our case, when the PS is present, the effective nonlinearity is reinforced by a factor 8 compared to the one of the simple chalcogenide layer. As a consequence, we have to take $n_{2,eff} = 8n_2$ in the above formula, with n_2 the chalcogenide nonlinear coefficient. In order to compare these theoretical results with our experimental data, we have extracted the distances from the left and right secondary lateral peaks relative to the central peak from the output beam profiles obtained for configuration II (see Figure 5

in the article) for the different intensity. The comparison is shown in Figure S12. The spatial period generated by the modulation instability is expected to be much larger than the experimental distance between the lateral secondary peaks and the central peak. If a smaller effective nonlinear coefficient ($\times 3.15$) is considered then, as expected, the difference is even larger. It is worth mentioning that in this figure the used beam intensity is the input one while it is known (see loss results in the Optical characterizations section of the article) that the actual beam intensity in the PS region is significantly smaller therefore the obtained differences between theoretical results from modulation instability and experimental ones are underestimated.

References

- (1) J. Charrier and M. L. Anne and H. Lhermite and V. Nazabal and J. P. Guin and F. Charpentier and T. Jouan and F. Henrio and D. Bosc and J. L. Adam., Sulphide $\text{Ga}_x\text{Ge}_{25-x}\text{Sb}_{10}\text{S}_{65(x=0,5)}$ sputtered films: Fabrication and optical characterizations of planar and rib optical waveguides. *Journal of Applied Physics* **2008**, *104*, 073110.
- (2) Elsayy, M. M. R.; Renversez, G. Exact calculation of the nonlinear characteristics of 2D isotropic and anisotropic waveguides. *Opt. Lett.* **2018**, *43*, 2446–2449.
- (3) Powers, P. E.; Haus, J. W. *Fundamentals of Nonlinear Optics*, 2nd ed.; CRC Press, 2017.
- (4) Akhmediev, N.; Ankiewicz, A.; Soto-Crespo, J. M. Does the nonlinear Schrödinger equation correctly describe beam propagation? *Opt. Lett.* **1993**, *18*, 411.
- (5) Chen, Y.; Atai, J. Maxwell's equations and the vector nonlinear Schrödinger equation. *Physical Review E* **1997**, *55*, 3652–3657.

- (6) Drouart, F.; Renversez, G.; Nicolet, A.; Geuzaine, C. Spatial Kerr solitons in optical fibers of finite size cross section: beyond the Townes soliton. *J. Opt. A: Pure Appl. Opt.* **2008**, *10*, 125101.
- (7) Agrawal, G. P. *Nonlinear fiber optics*, 3rd ed.; Academic Press, 2001.
- (8) Walasik, W. Plasmon–soliton waves in metal-nonlinear dielectric planar structures. PhD thesis, Aix-Marseille Université, 2014.
- (9) Taflove, A., Oskooi, A., Johnson, S. G., Eds. *Advances in FDTD Computational Electrodynamics*; Photonics and Nanotechnology; Artech House, Boston, 2013.
- (10) Hult, J. A Fourth-Order Runge-Kutta in the Interaction Picture Method for Simulating Supercontinuum Generation in Optical Fiber. *IEEE J. Lightwave Technol.* **2007**, *25*, 3770–3775.
- (11) O. V. Sinkin, J., R. Holzlohner; Menyuk, C. R. Optimization of the Split-Step Fourier Method in Modeling Optical Fiber Communications Systems. *IEEE J. Lightwave Technol.* **2003**, *21*, 61–68.
- (12) El-Amraoui, M.; Fatome, J.; Jules, J. C.; Kibler, B.; Gadret, G.; Fortier, C.; Smektala, F.; Skripatchev, I.; Polacchini, C.; Messaddeq, Y.; Troles, J.; Brilland, L.; Szpualak, M.; Renversez, G. Strong infrared spectral broadening in low-loss As-S chalcogenide suspended core microstructured optical fibers. *Opt. Express* **2010**, *18*, 4547–4556.
- (13) Falconieri, M.; Salvetti, G. Simultaneous measurement of pure-optical and thermo-optical nonlinearities induced by high-repetition-rate, femtosecond laser pulses: application to CS₂. *Applied Physics B* **1999**, *69*, 133–136.
- (14) Gnoli, A.; Razzari, L.; Righini, M. Z-scan measurements using high repetition rate lasers: how to manage thermal effects. *Opt. Express* **2005**, *13*, 7976–7981.

- (15) Falconieri, M. Thermo-optical effects in Z -scan measurements using high-repetition-rate lasers. *Journal of Optics A: Pure and Applied Optics* **1999**, *1*, 662–667.
- (16) Eggleton, B. J.; Poulton, C. G.; Rakich, P. T.; Steel, M. J.; Bahl, G. Brillouin integrated photonics. *Nature Photonics* **2019**, *13*, 664–677.
- (17) Kumari, V.; Kaswan, A.; Patidar, D.; Sharma, K.; Saxena, N. S. Effective thermal conductivity and diffusivity of GeSeSb glasses measured simultaneously as a function of temperature and fit to empirical equations. *Journal of Asian Ceramic Societies* **2015**, *3*, 339–344.
- (18) Olivier, M.; Tchahame, J.; Němec, P.; Chauvet, M.; Besse, V.; Cassagne, C.; Boudebs, G.; Renversez, G.; Boidin, R.; Baudet, E.; Nazabal, V. Structure, nonlinear properties, and photosensitivity of (GeSe₂)_{100-x}(Sb₂Se₃)_x glasses. *Opt. Mater. Express* **2014**, *4*, 525–540.
- (19) Kuriakose, T.; Baudet, E.; Halenkovič, T.; Elsayy, M. M.; Němec, P.; Nazabal, V.; Renversez, G.; Chauvet, M. Measurement of ultrafast optical Kerr effect of Ge-Sb-Se chalcogenide slab waveguides by the beam self-trapping technique. *Opt. Comm.* **2017**, *403*, 352 – 357.
- (20) Feigenbaum, E.; Orenstein, M. Plasmon–soliton. *Opt. Lett.* **2007**, *32*, 674.
- (21) Dauxois, T.; Peyrard, M. *Physics of Solitons*; Cambridge university Press, 2006.
- (22) Chauvet, M.; Fanjoux, G.; Huy, K. P.; Nazabal, V.; Charpentier, F.; Billeton, T.; Boudebs, G.; Cathelinaud, M.; Gorza, S.-P. Kerr spatial solitons in chalcogenide waveguides. *Opt. Lett.* **2009**, *34*, 1804–1806.
- (23) Malendevich, R.; Jankovic, L.; Stegeman, G.; Aitchison, J. S. Spatial modulation instability in a Kerr slab waveguide. *Opt. Lett.* **2001**, *26*, 1879–1881.